JSR Publications

Available Online

J. Sci. Res. **18** (2), 389-406 (2026)

JOURNAL OF SCIENTIFIC RESEARCH

www.banglajol.info/index.php/JSR

A Comprehensive Physical Insight into WC Polymorphs via First-Principles

M. M. Islam, H. Mikat, M. Islam*

Nuclear Safety, Security and Safeguard Division, Bangladesh Atomic Energy Regulatory Authority (BAERA), E-12/A, Agargaon, Dhaka-1207, Bangladesh

Received 11 September 2025, accepted in final revised form 25 January 2026

Abstract

Tungsten carbide (WC) has attracted immense attention for extreme-environment applications owing to its outstanding hardness, high melting point, thermal stability, and chemical inertness. First-principles calculations based on density functional theory (DFT) are performed to investigate the key physical properties of the cubic (α-WC) and hexagonal (β-WC) phases. The optimized lattice parameters show close agreement with reported values. The calculated negative formation energies indicate thermodynamic stability, and the phonon dispersion further reveals dynamical instability in α-WC at 0 K, in contrast to the absence of any imaginary modes in β-WC. They are both metallic polymorphs with no bandgaps (E_g = 0 eV). Both the phases exhibit mechanical stability and elastic anisotropy, with Vickers hardness of 30.96 GPa for the ductile α-WC and 62.86 GPa for the brittle β-WC. The Debye temperature of β-WC (670 K) is higher than that of α-WC (551 K), and the direct free energy of β-WC is more stable. Both the polymorphs exhibit ultrahigh melting temperatures. The β-WC possesses a much higher lattice thermal conductivity of 273 $Wm^{-1}K^{-1}$ at 300 K compared to 35 $Wm^{-1}K^{-1}$ for α-WC. These findings demonstrate that WC polymorphs are ideal candidates for ultrahigh-temperature applications, including nuclear, aerospace, and energy technologies.

Keywords: WC polymorphs; DFT; Phonon dynamics; Thermophysical properties; Mechanical hardness.

doi: https://dx.doi.org/10.3329/jsr.v18i2.84256 J. Sci. Res. 1**8** (2), 389-406 (2026)

1. Introduction

Transition metal carbides (TMCs) have attracted significant attention as an important class of materials due to their remarkable combination of ceramic-like hardness and metallic properties, including high electrical and thermal conductivity. Their exceptional mechanical strength, high melting points, excellent wear and corrosion resistance, and chemical stability enable reliable performance under extreme conditions of temperature, pressure, and radiation. These attributes make TMCs indispensable for cutting tools, wear-resistant coatings, aerospace and defence applications, and energy-related technologies, while their tunable bonding nature and polymorphic structures offer rich opportunities for tailoring

*Corresponding author: m.islam4399@gmail.com

physical properties [1–6]. Tungsten carbide (WC), a refractory transition metal carbide, has emerged as a strategically important material for applications operating under extreme conditions of temperature, stress, and radiation. Its exceptional mechanical strength, high hardness, elevated melting point, and outstanding wear resistance make it indispensable in cutting tools, wear-resistant coatings, and high-temperature structural components [6–10]. Beyond conventional industrial uses, WC has garnered significant interest in the nuclear technology domain, where materials must withstand intense neutron irradiation, severe thermal gradients, and chemically aggressive environments.

The high density and low thermal expansion of WC, coupled with its excellent thermal conductivity, offer unique advantages for potential deployment in advanced fission and fusion reactor systems, including roles as plasma-facing components, neutron absorbers, and structural elements in coolant circuits.

From a materials design perspective, WC's polymorphic forms—most notably the cubic (α-WC) and hexagonal (β-WC) phases—exhibit distinct structural, electronic, and elastic properties, which directly influence their mechanical and irradiation tolerance [9–13]. Several earlier works have explored WC polymorphs with an emphasis on their structural, electronic, elastic, and bonding properties [6–13]. However, a more comprehensive understanding is required to capture the essential physical characteristics of these phases. In the present investigation, we extend this scope by systematically examining the structural, electronic, stability, elastic, anisotropic, mechanical, thermodynamic, and thermophysical properties of WC polymorphs in detail.

Density functional theory (DFT)-based first-principles simulations have become indispensable in investigating such characteristics at the atomic scale, enabling accurate predictions of phase stability, defect energies, elastic anisotropy, and thermomechanical behavior under reactor-relevant conditions. These computational insights not only guide experimental efforts but also accelerate the screening and optimization of candidate materials for nuclear and aerospace applications, reducing reliance on time- and cost-intensive trial-and-error methods.

In this study, we employ DFT calculations to systematically explore the fundamental physical properties of WC polymorphs, with particular attention to their structural stability, mechanical performance, thermal transport, and electronic characteristics. By correlating these properties with operational demands in nuclear environments, the present work aims to provide a comprehensive understanding of WC's suitability and design potential for extreme-service applications. Such a computational framework will facilitate the rational development of next-generation nuclear materials that can ensure both safety and performance under the most demanding conditions.

2. Computational Approach

All the first-principles calculations in this work were carried out using the Cambridge Serial Total Energy Package (CASTEP) within the framework of density functional theory (DFT) [14]. The ultrasoft Vanderbilt-type plane-wave pseudopotential method was adopted to

describe the electron–ion interactions, while the exchange–correlation effects were treated using the generalized gradient approximation (GGA) in the PBESol parameterization, which is well-suited for accurate prediction of structural properties of solids [15,16]. The Kohn–Sham equations were solved self-consistently with iterative electronic minimization [17]. Structural optimization was carried out using the Broyden–Fletcher–Goldfarb–Shanno (BFGS) algorithm, with convergence thresholds set as follows: total energy 1.0×10^{-6} eV/atom, maximum force 0.03 eV/Å, maximum stress 0.05 GPa, and maximum displacement 0.001 Å [18]. The valence electron configurations considered were W: $5s^25p^65d^46s^2$ and C: $2s^22p^2$. To ensure reliable results, a sufficiently high plane-wave cutoff energy and Monkhorst–Pack k-point sampling was employed for Brillouin zone integration, with the mesh density chosen according to the crystal symmetry of each polymorph [19]. The elastic constants (C_{ij}) were obtained using the stress–strain approach, where minor finite distortions were applied to the equilibrium structures and the corresponding stress tensors were calculated [20]. From these constants, the polycrystalline mechanical properties, including bulk modulus (B), shear modulus (G), and Young's modulus (Y), were derived using the Voigt–Reuss–Hill (VRH) averaging scheme [21,22].

The phonon dispersion relations were computed through density functional perturbation theory (DFPT), and they reveal the vibrational stability and lattice dynamics of the compounds [23,24]. The thermodynamic properties, such as Debye temperature, free energy, entropy, and heat capacity, were subsequently evaluated based on the phonon density of states within the quasi-harmonic approximation. Furthermore, the thermophysical parameters, including melting temperature, sound velocities, Grüneisen parameter, and lattice thermal conductivity, were estimated using established empirical and theoretical models.

These computational frameworks ensure a comprehensive assessment of the structural, electronic, elastic, phononic, thermodynamic, and thermal transport properties of WC polymorphs, providing robust predictions relevant to their potential use in extreme-environment applications.

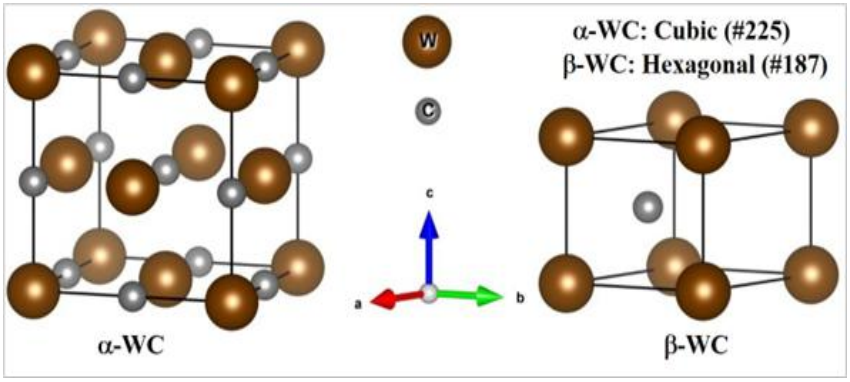

Fig. 1. The 3D optimized crystal structures of WC polymorphs.

Visualization of the fully relaxed three-dimensional crystal structure was carried out with the help of the VESTA software [25]. To investigate the material's elastic anisotropy, the ELATE online tool was employed [26], which enabled the generation of three-dimensional anisotropic plots for Young's modulus, shear modulus, and Poisson's ratio, offering a detailed insight into the elastic behavior of the material.

3. Results and Discussion

3.1. *Structural analysis*

The optimized crystal structures of α-WC and β-WC are shown in Fig. 1, and their structural parameters are summarized in Table 1. For α-WC, the crystal adopts a rock-salt type cubic structure (space group $Fm\bar{3}$m, #225), where tungsten and carbon atoms occupy the Wyckoff positions 4a (0, 0, 0) and 4b (1/2, 0, 0), respectively. The optimized lattice parameter of α-WC is a = 4.346 Å, giving a cell volume of 82.094 $Å^3$ (4 f.u. per cell), that lies very close to the previous study (4.35–4.398 Å) [9,12,27,28-30] and falls within the experimental window (4.220–4.266 Å) [9,12,31], confirming the reliability of our PBESol optimization. For the electronic structure calculations, a plane-wave energy cut-off of 550 eV and a Monkhorst–Pack k-point grid of 8×8×8 was used to ensure accurate Brillouin zone sampling. In the case of β-WC, the obtained structure is hexagonal (space group $P\bar{6}m2$, #187), where tungsten and carbon atoms are located at the Wyckoff positions 1a (0, 0, 0) and 1f (2/3, 1/3, ½), respectively. For β-WC, we obtain a = 2.901 Å, c = 2.828 Å, with c/a = 0.975 and cell volume 20.604 $Å^3$ (1 f.u. per cell). These metrics agree excellently with experiments (a ≈ 2.90–2.91 Å, c ≈ 2.83–2.84 Å, c/a ≈ 0.976) [10,11,13,31] and previous GGA calculations [7,9,10]. For the β-WC phase, the plane-wave energy cut-off was 450 eV, and the Brillouin zone was sampled with a 10×10×9 Monkhorst–Pack k-point mesh.

The formation energies, E_f = −10.809 eV/atom for α-WC and E_f = −11.277 eV/atom for β-WC, indicate that both polymorphs are energetically stable, with β-WC being slightly more favorable. The volumes per formula unit for α- and β-WC (≈20.52 $Å^3$ and 20.60 $Å^3$, respectively) are nearly identical, indicating comparable packing densities despite their different symmetries— a point relevant for assessing phase transformations under pressure or temperature.

$$\text{Formation energy, } E_f\,(WC) = \frac{[E(WC) - n_W E(W) - n_C E©]}{n_W + n_C}$$

Here, E(W) and E© denote the energies of W and C atoms, respectively, while E(WC) represents the total energy of the WC unit cell, with n_W and n_C being the numbers of constituent W and C atoms per unit cell. Table 2 confirms that both α-WC and β-WC exhibit zero bandgap (E_g = 0.00 eV), establishing their metallic nature. The unit cell of α-WC contains eight atoms (4 f.u.), while β-WC has two atoms (1 f.u.), reflecting their structural differences. In both phases, the calculated magnetic moment is 0.00 μB/f.u., confirming non-magnetic behavior.

Table 1. The chemical formula, optimization method, and geometrically relaxed unit structural parameters of WC polymorphs.

Compound	Simulation package	Approximation method	Lattice constant (Å)		c/a	Volume, V (Å^3)	Formation energy, E_f (eV/atom)	Remarks
			a	c				
Cubic WC (α–WC)	CASTEP	GGA-PBESOL	4.346	-	-	82.094	−10.809	This work
	-	Experimental	4.266	-	-	-	-	[9]
	-	Experimental	4.220	-	-	-	-	[12]
	-	Experimental	4.229	-	-	-	-	[12]
	-	Experimental	4.192	-	-	-	-	[31]
	DACAPO	GGA-PWPP	4.35	-	-	-	-	[12]
	CASTEP	GGA-PBE	4.351	-	-	82.3748	-	[29]
	-	-	4.32	-	-	-	-	[28]
	WIEN2k	GGA-PBE	4.398	-	-	-	-	[9]
		GGA-LDA	4.38	-	-	-	-	[27,30]
Hexagonal WC (β–WC)	CASTEP	GGA-PBESOL	2.901	2.828	0.975	20.604	−11.277	This work
	-	Experimental	2.906	2.8375	-	-	-	[13]
	-	Experimental	2.90	2.83	-	20.83	-	[10]
	-	Experimental	2.91	2.84	0.976	-	-	[11]
		Experimental	2.905	2.838	-	-	-	[31]
	CASTEP	GGA-PBE	2.91	2.84	-	20.97	-	[10]
	WIEN2k	GGA-PBE	2.926	2.849	-	-	-	[9]
	CASTEP	GGA-PBE	2.906	2.825	-	20.6558	-	[29]

Table 2. Electronic and magnetic parameters of WC polymorphs.

Compound	Bandgap, E_g (eV)	Electronic property	No. of atoms per unit cell	No. of formula units (f.u.) per unit cell	Magnetic moment, μ_{total} (μ_B/f.u.)	Remarks
α–WC	0.00	Metallic	8	4	0.00	This work
β–WC	0.00	Metallic	2	1	0.00	This work

3.2. *Electronic properties*

Fig. 2 presents the electronic band structures of cubic (α-WC) and hexagonal (β-WC) polymorphs along the high-symmetry points of their Brillouin zones. For α-WC, the conduction and valence bands strongly overlap at the Fermi level (E_F), with no discernible bandgap. Both spin-up and spin-down channels exhibit identical dispersions, confirming the non-magnetic metallic nature of this phase. The bands crossing E_F originate mainly from the hybridization between W-5d and C-2p states, which ensures a high electronic density near the Fermi level. This behavior is consistent with earlier reports [7,9,12,28,29,32,33] where metallic conduction in α-WC was attributed to strong covalent-metallic bonding between tungsten and carbon atoms. In the case of β-WC, a similar metallic character is observed with continuous band overlap at E_F, though Amy *et al.* concluded it is semi-metallic in nature [11]. However, the bandwidth in β-WC is much larger compared to α-WC, reflecting stronger orbital interactions and denser electronic states. The higher dispersion of bands in β-WC suggests enhanced electronic conductivity, which agrees with its superior stability as predicted by formation energy calculations [33]. Moreover, the

absence of spin-splitting again indicates a non-magnetic ground state, consistent with the zero total magnetic moment obtained from our structural analysis. Thus, β-WC not only represents the thermodynamically stable phase but also promises better electron transport properties, crucial for advanced industrial and nuclear applications.

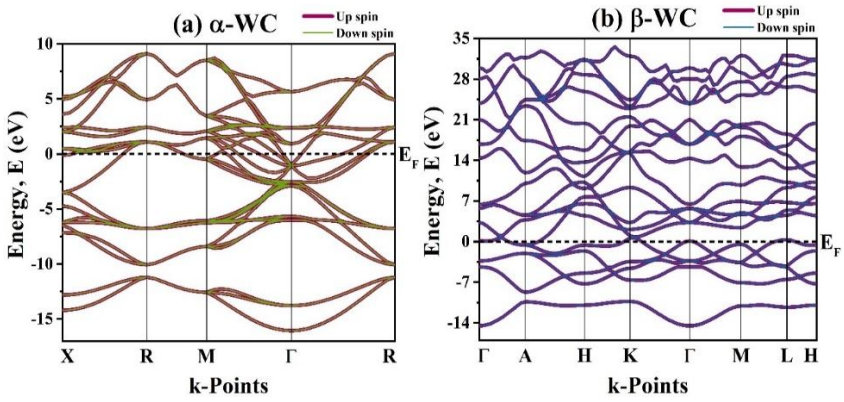

Fig. 2. The electronic band spectra of (a) cubic and (b) hexagonal WC.

Fig. 3 illustrates the total and partial density of states (DOS) for both cubic (α-WC) and hexagonal (β-WC) polymorphs of tungsten carbide, thereby offering insight into their electronic structures and bonding nature. Fig. 3(a) reveals that both cubic α-WC and hexagonal β-WC exhibit a finite density of states at the Fermi level (E_F), confirming their metallic nature. However, the DOS intensity at E_F in α-WC (3.4 states/eV) is significantly higher compared to β-WC (0.24 states/eV), implying stronger metallic conductivity in the cubic polymorph. This finding is consistent with earlier theoretical reports [9,11,28,29,33], which suggested that variations in structural symmetry directly influence the electronic bandwidth and metallic strength in transition metal carbides. The comparatively lower DOS of β-WC at E_F indicates reduced carrier concentration, thereby rationalizing its superior phase stability but relatively weaker electrical conductivity. The spin density distributions presented in Fig. 3 exhibit symmetric and oppositely aligned spin channels, which cancel each other out. This behavior clearly confirms the non-magnetic ground state of both α-WC and β-WC polymorphs, consistent with their metallic bonding nature and absence of unpaired d-electrons.

Fig. 3(b) reveals the states near E_F are predominantly derived from the W-5d orbitals, while the C-2p orbitals strongly hybridize with W-5d states in the energy window between −8 eV and −2 eV in α-WC. Such d–p hybridization underpins the robust covalent–metallic bonding that imparts α-WC with high hardness, ductility, and wear resistance. The dominance of W-5d states at E_F ensures metallic conduction, while the hybridization peaks reflect substantial interatomic orbital overlap, consistent with earlier DFT studies on carbides [9,29,33]. The higher DOS at E_F in α-WC suggests its potential applicability in

electrical contact materials, cutting tools, and thermal conductors, where robust charge carrier transport is essential.

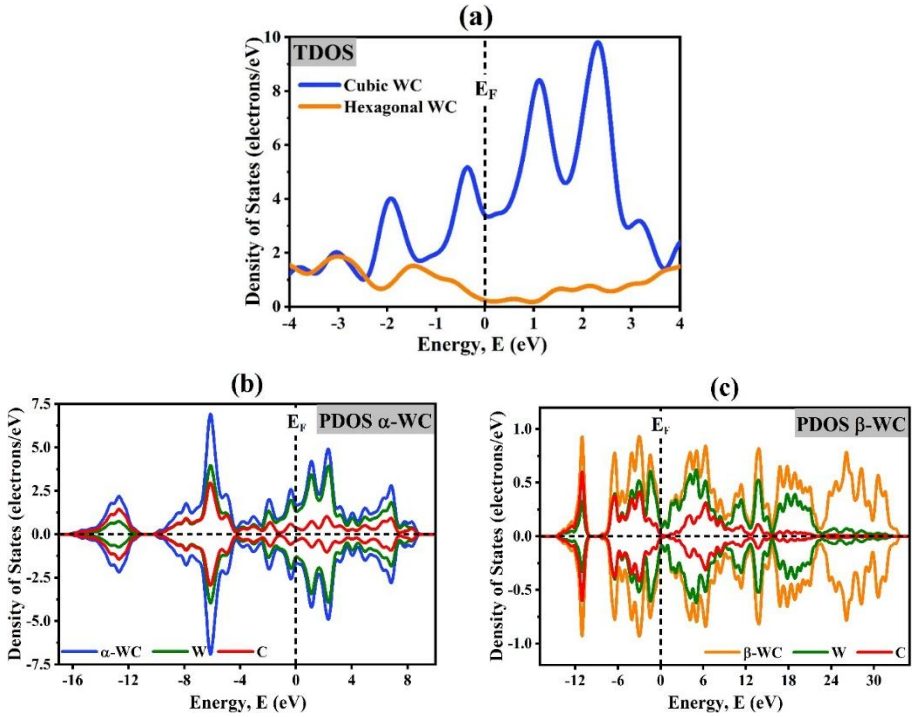

Fig. 3. The (a) total DOS of WC polymorphs, (b) partial DOS of α-WC, and (c) partial DOS of β-WC.

Fig. 3(c) reveals that a similar hybridization between W-5d and C-2p orbitals is observed, though with a broader energy spread in β-WC. W-5d orbitals remain dominant near E_F. Importantly, the DOS intensity at E_F is lower than that of α-WC, which aligns with its lower metallic conductivity but higher thermodynamic stability [9,29]. Such electronic behavior explains the brittleness of β-WC, as stronger covalent interactions restrict dislocation mobility despite ensuring high hardness. This balance of bonding characteristics makes β-WC a promising candidate for high-temperature structural applications and wear-resistant coatings, where hardness and thermal stability are critical.

3.3. *Elastic and mechanical characteristics*

In this study, the elastic constants and the corresponding moduli were evaluated using the stress–strain method as implemented in the CASTEP simulation package. The determination of key mechanical parameters such as bulk modulus (B), shear modulus (G), Young's modulus (Y), Pugh's ratio (B/G), Vickers hardness (H_V), machinability index (B/C_{44}), and Poisson's ratio (ν) is essential for assessing the practical applicability of

materials in engineering and industrial environments. The bulk, shear, and Young's moduli were derived from the computed single-crystal elastic constants (C_{ij}) by employing the Voigt–Reuss–Hill (VRH) averaging scheme, which provides a reliable estimate of the polycrystalline response by combining the theoretical upper and lower bounds of elastic behavior [20-22,34-40].The calculated elastic stiffness constants (C_{ij}) of α-WC and β-WC are listed in Table 3, together with earlier reports. For α-WC, the longitudinal elastic constant C_{11} = 871.27 GPa is significantly larger than the transverse constant C_{12} = 149.42 GPa, reflecting its strong directional bonding and anisotropic stiffness. These values are in close agreement with previous theoretical predictions (C_{11} = 706.5 GPa, C_{12} = 191.4 GPa) [9,29]. For β-WC, the corresponding constants are C_{11} = 764.07 GPa and C_{12} = 223.19 GPa, again consistent with earlier values [9,29]. The high magnitude of C_{33} = 1009.05 GPa in β-WC compared with α-WC highlights the strong covalent bonding along the c-axis in the hexagonal lattice. The C_{44} shear constants of α-WC and β-WC are 139.43 GPa and 324.33 GPa, respectively, both comparable with reported data [9,29]. The calculated Cauchy pressure ($C_P = C_{12}-C_{44}$) is positive for α-WC (9.99 GPa), indicating ductile behavior. In contrast, for β-WC ($C_P = C_{13}-C_{44}$), it is highly negative (−144.32 GPa), suggesting strong directional covalent bonds and brittleness. Both polymorphs satisfy Born's stability criteria, confirming mechanical stability in agreement with earlier work [9,29,41]. According to Born–Huang's lattice dynamical theory, the mechanical stability criteria can be expressed as [39-41]:

Hexagonal system (for β-WC): $C_{11}>0$, $C_{44}>0$, $(C_{11}-C_{12})>0$, $(C_{11}+C_{12})\,C_{33}>2C^2_{13}$

Cubic system (for α-WC): $C_{11}>0$, $C_{44}>0$, $C_{11}-C_{12}>0$, $C_{11}+2C_{12}>0$

Table 3. Elastic stiffness constants (C_{ij}), Cauchy pressure (C_P), and mechanical stability of WC polymorphs.

Properties	α-WC		β-WC	
	This work	Previous study	This work	Previous study
C_{11} (GPa)	871.27	706.5 [9] 696.5 [29]	764.07	772.8 [9] 711.6 [29] 720 [41]
C_{12} (GPa)	149.42	191.4 [9] 215.5 [29]	223.19	209.9 [9] 240.6 [29] 254 [41]
C_{13} (GPa)	-	-	180.01	157.8 [9] 168 [29] 267 [41]
C_{33} (GPa)	-	-	1009.05	960.6 [9] 977.5 [29] 972 [41]
C_{44} (GPa)	139.43	151.6 [9] 122 [29]	324.33	302.2 [9] 305.1 [29] 328 [41]
C_P (GPa)	9.99	-	−144.32	-
Mechanical stability	Stable	Stable [9]	Stable	Stable [8] Stable [9]

The bulk modulus (B) is found to be 390 GPa for α-WC and 410 GPa for β-WC, consistent with earlier studies (B ≈ 363–434 GPa) [9,10]. The shear modulus (G) is significantly higher in β-WC (311 GPa) compared with α-WC (206 GPa), which explains the superior hardness of the hexagonal phase. Similarly, the Young's modulus (Y) of β-WC (745 GPa) far exceeds that of α-WC (526 GPa), confirming its stiffer mechanical response. The calculated Vickers hardness (H_V) clearly distinguishes the two polymorphs: 30.9 GPa for α-WC, which is comparable to other tough refractory carbides, and a much higher 62.9 GPa for β-WC,

categorizing it among superhard materials. This observation is consistent with prior experimental and theoretical studies [9,10], which also reported β-WC to be harder and more brittle. The machinability index (B/C_{44}) reflects a material's ease of machining, with higher values indicating better workability. For cubic α-WC, B/C_{44} is 2.80, suggesting relatively satisfactory machinability despite its hardness, whereas β-WC shows a much lower value of 1.26, consistent with its brittle nature and strong resistance to shear deformation. This contrast highlights α-WC as more workable in machining applications, while β-WC is better suited for wear-resistant structural uses. The B/G ratio of α-WC (1.89) exceeds the critical value of 1.75, indicating ductile character, while that of β-WC (1.32) suggests brittleness. This is also supported by Poisson's ratio (σ), which is 0.275 for α-WC (ductile) and 0.197 for β-WC (brittle). The calculated anisotropy index (A^U) values (1.169 for α-WC, 0.102 for β-WC) indicate that the cubic phase is more anisotropic than the hexagonal one, which is also in agreement with the earlier work [9].

Table 4. Elastic moduli (B, G, Y), Pugh's ratio (B/G), Vickers hardness (H_V), machinability index (B/C_{44}), Poisson's ratio ((σ), international anisotropy index (A^U), and nature of WC polymorphs.

Properties	α-WC		β-WC	
	This work	Previous study	This work	Previous study
B (GPa)	390.04	363.1 [9] 375.9 [29] 396[27]	409.54	382.4 [9] 393 [29] 434 [10]
G (GPa)	206.41	187.7 [9] 160.7 [29]	311.24	294.6 [9] 286.2 [29]
Y (GPa)	526.38	480.4 [9] 422.7 [29]	745.00	703.2 [9] 690.9 [29]
B/G	1.89	1.93 [9] 2.34 [29]	1.32	1.29 [9] 1.37 [29]
H_V (GPa)	30.96	-	62.86	-
B/C_{44}	2.80	-	1.26	-
σ	0.275	0.279 [9] 0.313 [29]	0.197	0.194 [9] 0.207 [29]
A^U	1.169	-	0.102	-
Nature	Ductile	Ductile [9]	Brittle	Brittle [9]

The anisotropic nature of the elastic properties of α-WC and β-WC was assessed using three-dimensional representations of Young's modulus (Y), shear modulus (G), and Poisson's ratio (σ) in Fig. 4, along with the numerical anisotropy factors presented in Table 5. The visualizations highlight the inherent directional dependence of the mechanical properties, which is crucial for assessing the mechanical reliability of these carbides under operational stresses.

Table 5. The minimum and maximum limit of Young's modulus (Y), Shear modulus (G) and Poisson's ratio ((σ) of WC polymorphs.

Compd.	Young's modulus (GPa)			Shear modulus (GPa)			Poisson's ratio		
	Y_{min}	Y_{max}	Anisotropy	G_{min}	G_{max}	Anisotropy	σ_{min}	σ_{max}	Anisotropy
α–WC	373.76	827.53	2.214	139.43	360.93	2.589	0.077	0.553	7.220
β–WC	682.08	943.40	1.383	270.44	343.3	1.270	0.132	0.261	1.980

For α-WC, the 3D surfaces of Y and G are highly distorted, with pronounced lobes in specific crystallographic directions that reflect strong anisotropy in elastic stiffness and shear resistance. The upper and lower values of Y, G, and are presented in Table 5, where Y varies widely from 373.76 to 827.53 GPa (anisotropy ratio ≈ 2.21) and G from 139.43 to 360.93 GPa (anisotropy ratio ≈ 2.59). Such significant directional dependence is attributed to the cubic lattice geometry coupled with directional W-C covalent bonding. The Poisson's ratios (σ) also exhibit large anisotropies, ranging from 0.077 to 0.553, corresponding to a ratio of ≈ 7.22, which suggests that the ductility of α-WC is strongly orientation-dependent, with some crystallographic directions being much more deformable than others.

In contrast, β-WC displays nearly spherical 3D surfaces for all three moduli, reflecting an almost isotropic mechanical response. The Young's modulus varies narrowly from 682.08 to 943.40 GPa (anisotropy ratio ≈ 1.38), and the shear modulus spans 270.44 to 343.33 GPa (anisotropy ratio ≈ 1.27). Similarly, Poisson's ratio varies only modestly between 0.132 and 0.261 (anisotropy ratio ≈ 1.98). These values confirm that β-WC exhibits much lower elastic anisotropy than α-WC. The isotropic nature of β-WC is a direct consequence of its hexagonal symmetry, which distributes bonding interactions more uniformly across crystallographic directions. Poisson's ratio also remains relatively uniform (0.132–0.261), consistent with the hexagonal crystal symmetry that distributes stresses more evenly across directions. This relatively lower anisotropy implies that β-WC may show more uniform mechanical behavior under multi-axial stress states, albeit at the cost of brittleness.

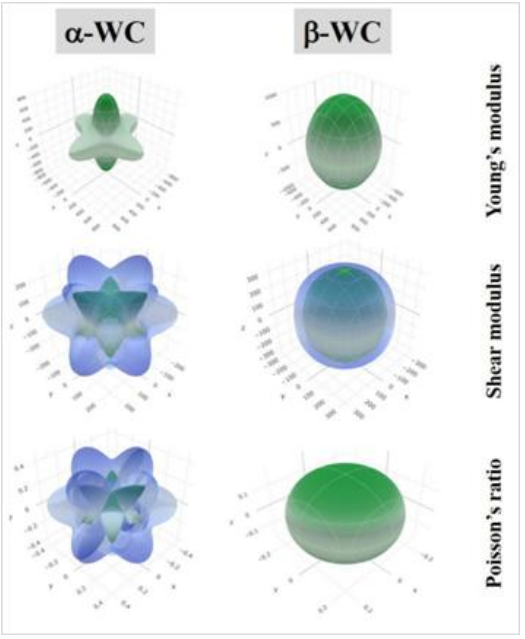

Fig. 4. The anisotropic 3D visualization of Young's modulus, shear modulus, and Poisson's ratio of WC polymorphs.

The clear difference between the polymorphs implies that while α-WC is directionally dependent and may show enhanced ductility in specific orientations, its anisotropy could lead to mechanical weakness under multi-axial stress conditions. On the other hand, β-WC, with its isotropic and stiffer elastic response than α-WC, is inherently more reliable for structural applications demanding uniform performance under complex loading, such as high-pressure cutting tools, wear-resistant coatings, and nuclear reactor components.

3.4. *Phonon dynamics*

The phonon dispersion spectra of α-WC and β-WC are depicted in Fig. 5. The phonon dispersion spectra of α-WC and β-WC provide crucial insights into their dynamical stability and lattice vibrational behavior. For α-WC, the dispersion relation shows that several branches extend into the imaginary frequency region (represented as negative values in red), particularly along the X–R–M–Γ–R symmetry directions. The occurrence of imaginary phonon modes indicates dynamical instability of the cubic phase at ambient conditions (0 K), even though it is mechanically and thermodynamically stable (Table 1, Table 3). This result is consistent with earlier studies on transition-metal carbides [30,42]. The maximum phonon frequencies in α-WC reach up to nearly 18 THz, reflecting strong W-C covalent bonding interactions. However, the presence of soft modes suggests that these bonds cannot fully stabilize the cubic lattice, thereby limiting its bulk applications.

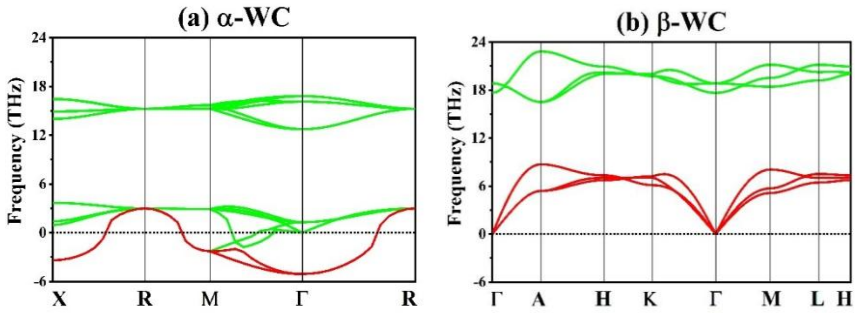

Fig. 5. The phonon dispersion curves of (a) cubic and (b) hexagonal WC.

In contrast, the β-WC phase exhibits a completely positive phonon spectrum, with no imaginary frequencies observed along the entire Γ–A–H–K–Γ–M–L–H path, confirming its dynamical stability [43-45], in agreement with the thermodynamic findings from formation energy calculations. The highest optical phonon modes also extend up to ~22 THz, consistent with strong bonding stiffness between tungsten and carbon atoms. The distinct separation between acoustic and optical branches suggests significant mass contrast between W and C atoms, which governs the vibrational behavior. The acoustic branches are linear near the Γ-point, further verifying lattice stability and sound velocity consistency. Notably, β-WC shows higher optical phonon frequencies, reflecting stronger W-C bond strength compared to α-WC. The stable phonon behavior of β-WC makes it an ideal

candidate for high-temperature structural materials, thermal barrier coatings, and nuclear reactor environments, where lattice stability under vibrational excitations is essential. On the other hand, the unstable α-WC phase retains importance in nanostructured coatings, electronic contacts, and complex protective layers, where non-equilibrium processing routes can stabilize it at reduced dimensions.

3.5. *Thermodynamic characteristics*

The temperature-dependent thermodynamic properties of the cubic (α-WC) and hexagonal (β-WC) polymorphs of tungsten carbide were investigated and plotted in Fig. 6 to gain insights into their lattice dynamics and thermal stability. The variation of Debye temperature (θ_D) with temperature in Fig. 6(a) highlights the remarkable difference in vibrational behavior between the two polymorphs. For α-WC, θ_D shows a steep and nearly linear rise with increasing temperature, eventually reaching values above 5000 K at higher temperatures. This indicates the presence of high-frequency phonon modes and strong interatomic bonding, which collectively contribute to its structural rigidity and superior mechanical stability. In contrast, β-WC exhibits a much lower θ_D, remaining almost constant beyond 600 K. The nearly flat profile of β-WC suggests relatively weaker phonon contributions and softer lattice dynamics, which may influence its thermal conductivity and stability under extreme conditions.

The enthalpy (H) as a function of temperature in Fig. 6(b) follows an expected monotonic increase for both polymorphs, reflecting the progressive accumulation of thermal energy in the lattice. However, the enthalpy of α-WC grows at a significantly higher rate compared to β-WC, consistent with its larger vibrational energy storage capacity. This higher enthalpy rise is in agreement with the elevated Debye temperature of α-WC, further confirming its ability to retain more thermal energy due to stronger bonding interactions.

The entropy contribution, represented as T*entropy in Fig. 6(c), displays a monotonic increase with temperature for both WC polymorphs. For α-WC, T*entropy rises steeply, reaching nearly 16 eV at 3000 K, while β-WC exhibits a more gradual increase, attaining only about 5 eV in the same range. The higher entropy values in α-WC indicate greater vibrational disorder and higher phonon excitation, which correlate with its larger Debye temperature and higher heat capacity. The lower entropy of β-WC, on the other hand, reflects stronger lattice stability and comparatively restricted phonon activity. Such entropy behavior is significant in understanding the thermal tolerance of these phases under high-temperature conditions.

Fig. 6(d) shows the variation of Helmholtz free energy with temperature. At 0 K, the free energy includes the zero-point energy (ZPE) contribution, calculated as 0.4211 eV for α-WC and 0.1601 eV for β-WC. With increasing temperature, the free energy of both polymorphs decreases due to the dominance of vibrational contributions, but the rate of decrease is more pronounced for α-WC. At 3000 K, α-WC reaches a free energy of nearly −12 eV, while β-WC maintains a higher free energy of about −5 eV. This stronger decline

in α-WC suggests that, despite its high melting temperature and vibrational stiffness, it is thermodynamically less favorable than β-WC under equilibrium conditions.

The heat capacity (C_V) in Fig. 6(e) exhibits the typical saturation behavior described by the Dulong–Petit law at elevated temperatures. For α-WC, C_V increases sharply at lower temperatures and reaches a plateau near 40 cal/cell·K, while β-WC attains a much lower saturation value of approximately 12 cal/cell·K. The pronounced difference in the saturation values highlights the influence of crystal structure and bonding characteristics on vibrational contributions to the heat capacity. The rapid approach of α-WC to its saturation value also indicates its higher vibrational density of states and stronger phonon-phonon interactions compared to β-WC.

The thermodynamic analysis demonstrates that α-WC possesses superior vibrational stiffness, higher energy storage capacity, and enhanced thermal stability relative to β-WC. These features make α-WC more suitable for applications demanding high-temperature resilience, whereas β-WC, with its lower θ_D, enthalpy, and C_V, may exhibit comparatively limited stability in extreme environments.

3.6. *Thermophysical properties*

Table 6 highlights the contrasting thermophysical behaviors of α-WC and β-WC. The melting temperature (T) exhibits a direct correlation with the elastic constants. In the case of cubic crystals, T_m can be computed utilizing the subsequent empirical formula [37,38,46]:

$$T_m = 553 + 5.91C_{11} \pm 300 \text{ K}$$

and T_m for the hexagonal crystal systems can be evaluated from the following relation [37,38]:

$$T_m = 354 + 3C_{11} + 1.5C_{33} \pm 300 \text{ K}$$

The predicted melting temperatures are extremely high, 5702 K for α-WC and 4160 K for β-WC, demonstrating their ability to operate under extreme thermal environments. The mass densities of 15847 kg/m^3 (α-WC) and 15785 kg/m^3 (β-WC) closely match experimental values [8,9,29], confirming the reliability of our calculations. The calculated Debye temperatures are 551 K for α-WC and 670 K for β-WC, in excellent agreement with reported values [8,11,29], with the higher value for β-WC reflecting stronger W–C bonding. Similarly, the average sound velocity (v_m) is higher for β-WC (4900 m/s) than for α-WC (4019 m/s), consistent with its superior stiffness [29]. The calculated densities (15847 kg/m^3 for α-WC and 15785 kg/m^3 for β-WC) match closely with experimental reports [8,9], while the Grüneisen parameter (γ) is slightly lower for β-WC (1.274 for β-WC and 1.628 for α-WC), suggesting reduced anharmonicity and better thermal transport. A striking difference is observed in the lattice thermal conductivity (k_L) at 300 K: α-WC shows only 35 Wm^{-1}K^{-1}, while β-WC exhibits an exceptionally high 273 Wm^{-1}K^{-1}. These results imply that α-WC, with a higher melting point and ductility, is more suited for applications requiring thermal stability and toughness, whereas β-WC, with superior thermal conductivity, is ideal for

nuclear reactor components, fusion plasma-facing materials, and thermal barrier systems where efficient heat dissipation is essential.

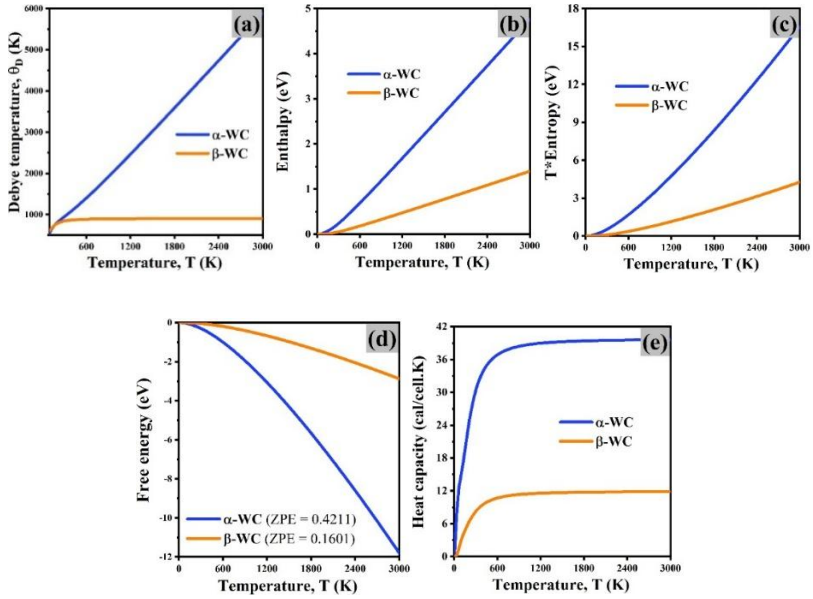

Fig. 6. Temperature-dependent thermodynamic properties of WC polymorphs: (a) Debye temperature, (b) enthalpy, (c) T*entropy, (d) free energy, and (e) heat capacity.

Table 6. The calculated melting temperature (T_m), cubic root of average atomic volume (δ), Grüneisen parameter (γ), molecular weight (M), mass density (ρ), average acoustic velocity (v_m), constant (A), Debye temperature (θ_D), minimum thermal conductivity (k_{min}), average atomic mass (M_{av}), and lattice thermal conductivity (k_L) of WC polymorphs.

Properties	α-WC		β-WC	
	This work	Previous study	This work	Previous study
Tm ± 300 (K)	5702	-	4160	-
$\delta \times 10^{-10}$ (m)	2.173	-	2.176	-
γ	1.628		1.274	-
M (kg/mol)	0.19585	-	0.19585	-
ρ (kg/m^3)	15847	15292 [9] 15790 [29]	15785	15965 [8] 15395 [9] 15740 [29]
vm (m/s)	4019	3569.0106 [29]	4900	4710.2989 [29]
$A \times 10^7$	3.152	-	3.294	-
θ_D (K)	551	448.49 [29]	670	660.30 [8] 621 [11]
k_{min} (Wm^{-1}K^{-1})	1.18	-	1.43	-
M_{av} (kg/mole)	0.09792	-	0.09792	-
k_L (at 300 K) (Wm^{-1}K^{-1})	35.28	-	273.11	-

The thermophysical response of the WC polymorphs, namely α-WC and β-WC, offers important details about their stability and suitability for high-temperature applications. Fig. 7 depicts the variation of lattice thermal conductivity (k_L) as a function of temperature, while Fig. 8 presents a comparative view of melting temperature (T_m) and k_L at room temperature (300 K). The calculated temperature-dependent lattice thermal conductivity demonstrates a clear inverse correlation with temperature for both polymorphs, a typical behavior attributed to enhanced phonon–phonon scattering at elevated temperatures. At low temperatures, β-WC exhibits remarkably high k_L values, exceeding 400 $Wm^{-1}K^{-1}$, which gradually decrease with increasing temperature, converging towards lower values at high-T regimes. In contrast, α-WC shows significantly reduced k_L values throughout the studied temperature range, with room-temperature k_L around 35.28 $Wm^{-1}K^{-1}$. This contrast highlights the superior phonon transport capability of β-WC, suggesting its potential as an efficient thermal conductor in extreme environments, whereas α-WC is comparatively more resistive to heat transport and may possess applications in thermal barrier contexts.

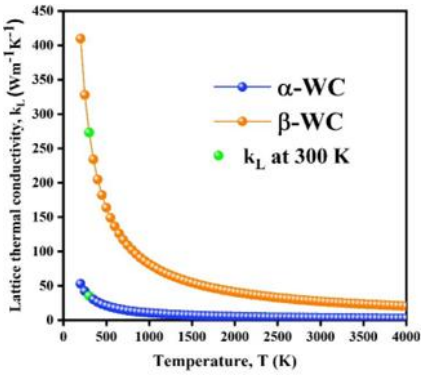

Fig. 7. Temperature-dependent behavior of lattice thermal conductivity (kL) in WC polymorphs.

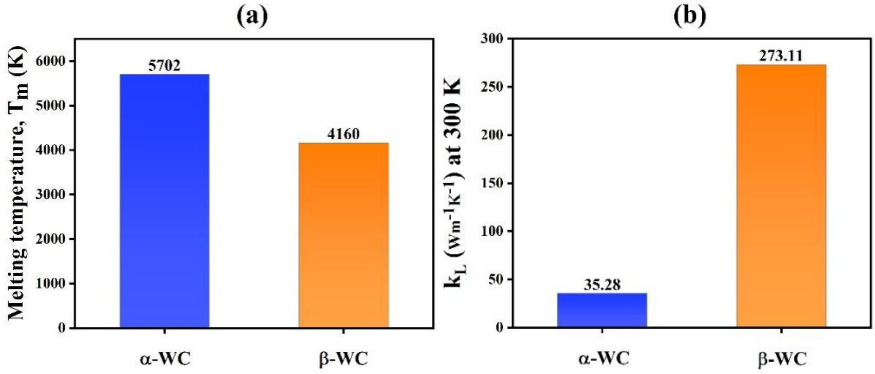

Fig. 8. Comparison of (a) melting temperatures, and (b) lattice thermal conductivity at 300 K among WC polymorphs.

Fig. 8(a) reveals that the melting temperature of α-WC (5702 K) is higher than that of β-WC (4160 K), underlining its superior structural and thermal stability. Such a high T_m

makes α-WC highly attractive for ultrahigh-temperature structural applications, including cutting tools, coatings, and reactor materials, where resistance to melting and creep is essential. Conversely, the relatively lower T_m of β-WC indicates its suitability in applications where thermal conductivity is prioritized over extreme thermal endurance. Fig. 8(b) further reinforces this contrasting behavior, showing that at 300 K, β-WC possesses a much higher k_L (273.11 $Wm^{-1}K^{-1}$) compared to α-WC (35.28 $Wm^{-1}K^{-1}$). This value suggests that β-WC may serve as a superior candidate in thermomechanical systems where rapid dissipation of heat is required, while α-WC may serve better in systems where controlled heat retention is desirable. Overall, these results establish a clear trade-off between thermal conductivity and melting temperature in the WC polymorphs. The high T_m of α-WC underscores its superior structural robustness, while the exceptional k_L of β-WC highlights its strong phonon transport efficiency. Such complementary characteristics suggest that tailored utilization of WC polymorphs could meet diverse engineering demands ranging from high-temperature stability to thermal management applications in advanced devices.

4. Conclusion

A thorough DFT analysis has been performed to examine the correlation between the structure and properties of WC polymorphs. The structural parameters of the optimized unit cells are a = 4.346 Å for α-WC and a = 2.901 Å, c = 2.828 Å for β-WC, which are consistent with previous investigations. The formation energies (−10.809 eV/atom for α-WC and −11.277 eV/atom for β-WC) and phonon dispersions affirm the superior thermodynamic and lattice dynamical stability of β-WC over α-WC. Both polymorphs have a metallic character (E_g = 0 eV) driven by the strong hybridization between W-5d and C-2p orbitals. The mechanical properties show that the bulk and shear moduli of α-WC reached about 390 and 206 GPa, and the corresponding values for β-WC were about 410 and 311 GPa. The ductility and brittleness of both WC phases (α-WC with B/G = 1.89 and β-WC with B/G = 1.32) have been classified by them as well as their Vickers hardness (30.96 GPa and 62.86 GPa). The Debye temperature (α-WC: 551 K and β-WC: 670 K) and the zero-point energy (α-WC: 0.421 eV and β-WC: 0.160 eV) are other thermodynamic quantities that clearly separate the two phases. Thermophysical analysis emphasizes that there is a trade-off: α-WC has an ultrahigh melting point (5702 K) and low lattice thermal conductivity (35 $Wm^{-1}k^{-1}$), and β-WC has a lower melting temperature (4160 K) but has much better thermal conductivity (273 $Wm^{-1}k^{-1}$ at 300 K). The complementary features suggest that α-WC could be used for ultrahigh-temperature and wear-resisting applications, and β-WC could be used for nuclear reactors, aerospace coatings, and energy-related thermal management applications. The present findings provide a robust theoretical framework for tailoring WC polymorphs to specific industrial requirements.

References

1. R. Ahmed, M. Mahamudujjaman, M. A. Afzal, M. S. Islam, R. S. Islam, and S. H. Naqib, J. Mater. Res. Tech. **24**, 4808 (2023). https://doi.org/10.1016/j.jmrt.2023.04.147
2. Y. Kim and B. Lee, Acta materialia **56**, 3481 (2008). https://doi.org/10.1016/j.actamat.2008.03.027
3. A. Friedrich, B. Winkler, E. A. Juarez-Arellano, and L. Bayarjargal, Materials **4**, 1648 (2011). https://doi.org/10.3390/ma4101648
4. T. Matsuda and H. Matsubara, J. Alloy Comp. **562**, 90 (2013). https://doi.org/10.1016/j.jallcom.2013.02.052
5. W. S. Williams, Mater. Sci. Eng.: A **105**, 1 (1988). https://doi.org/10.1016/0025-5416(88)90474-0
6. S. A. E. Johansson and G. Wahnström, Act. Mater. **59**, 171 (2011). https://doi.org/10.1016/j.actamat.2010.09.021
7. N. Jin, Y. Yang, X. Luo, S. Liu, Z. Xiao, P. Guo, and B. Huang, App. Surf. Sci. **324**, 205 (2015). https://doi.org/10.1016/j.apsusc.2014.10.119
8. J. Kim, Y. J. Suh, and I. Kang, J. Alloy. Comp. **656**, 213 (2016). https://doi.org/10.1016/j.jallcom.2015.09.214
9. D. V. Suetin, I. R. Shein, and A. L. Ivanovskii, Phys. Stat. Sol. **245**, 1590 (2008). https://doi.org/10.1002/pssb.200844077
10. Z. Shi, S. Liu, Y. Zhou, and Q. Yang, J. Phys. Chem. Sol. **123**, 11 (2018). https://doi.org/10.1016/j.jpcs.2018.07.007
11. A. Y. Liu, R. M. Wentzcovitch, and M. L. Cohen, Phys. Rev. B **38**, ID 9483 (1988). https://doi.org/10.1103/PhysRevB.38.9483
12. M. Christensen, S. Dudiy, and G. Wahnström, Phys. Rev. B **65**, ID 045408 (2002). https://doi.org/10.1103/PhysRevB.65.045408
13. A. S. Kurlov and A. I. Gusev, Inorg. Mater. **42**, 121 (2006). https://doi.org/10.1134/S0020168506020051
14. S. J. Clark, M. D. Segall, C. J. Pickard, P. J. Hasnip, M. I. Probert, K. Refson, and M. C. Payne, Z. Kristallogr. Cryst. Mater. **220**, 567 (2005). https://doi.org/10.1524/zkri.220.5.567.65075
15. D. Vanderbilt, Phys. Rev. B **41**, 7892 (1990). https://doi.org/10.1103/PhysRevB.41.7892
16. John P. Perdew, K. Burke, and M. Ernzerhof, Phys. Rev. Let. **77**, ID 3865 (1996). https://doi.org/10.1103/PhysRevLett.77.3865
17. W. Kohn and L. J. Sham, Phys. Rev. **140**, ID A1133 (1965). https://doi.org/10.1103/PhysRev.140.A1133
18. T. H. Fischer and J. Almlof, The J. Phys. Chem. **96**, 9768 (1992). https://doi.org/10.1021/j100203a036
19. H. J. Monkhorst and J. D. Pack, Phys. Revi. B **13**, ID 5188 (1976). https://doi.org/10.1103/PhysRevB.13.5188
20. O. H. Nielsen and R. M. Martin, Phys. Rev. Let. **50**, 697 (1983). https://doi.org/10.1103/PhysRevLett.50.697
21. R. Hill, Proc. Phys. Soc. Sec. A **65**, 349 (1952). https://doi.org/10.1088/0370-1298/65/5/307
22. H. Zvi and S. Shtrikman, J. Mech. Phys. Sol. **11**, 127 (1963). https://doi.org/10.1016/0022-5096(63)90060-7
23. G. Kresse, J. Furthmüller, and J. Hafner, Europhys. Let. **32**, 729 (1995). https://doi.org/10.1209/0295-5075/32/9/005
24. K. Parlinski, Z. Q. Li, and Y. Kawazoe, Phys. Rev. Let. **78**, 4063 (1997). https://doi.org/10.1103/PhysRevLett.78.4063
25. K. Momma and F. Izumi, J. Appl. Crystal. **44**, 1272 (2011). https://doi.org/10.1107/S0021889811038970
26. R. Gaillac, P. Pullumbi, and F. Coudert, J. Phys.: Cond. Mat. **28**, ID 275201 (2016). https://doi.org/10.1088/0953-8984/28/27/275201

27. J. C. Grossman, A. Mizel, M. Côté, M. L. Cohen, and S. G. Louie, Phys. Rev. B **60**, 6343 (1999). https://doi.org/10.1103/PhysRevB.60.6343
28. A. Y. Liu and M. L. Cohen, Sol. Stat. Comm. **67**, 907 (1988). https://doi.org/10.1016/0038-1098(88)90454-1
29. Y. Li, Y. Gao, B. Xiao, T. Min, Z. Fan, S. Ma, and L. Xu, J. Alloy Comp. **502**, 28 (2010). https://doi.org/10.1016/j.jallcom.2010.04.184
30. E. I. Isaev, S. I. Simak, I. A. Abrikosov, R. Ahuja, Y. K. Vekilov, M. I. Katsnelson, A. I. Lichtenstein, and B. Johansson, J. App. Phys. **101**, 123519 (2007). https://doi.org/10.1063/1.2747230
31. A. M. Nartowski, I. Parkin, and A. Craven, J. Mater. Chem. **9**, 1275 (1999). https://doi.org/10.1039/A808642g
32. R. Mathrubutham, P. Saigeetha, G. Kalpana G. Kalpana and B. P. B. Palanivel, Jap. J. App. Phys. **33**, 1847 (1994). https://doi.org/10.1143/JJAP.33.1847
33. D. V. Suetin, I. R. Shein, and A. L. Ivanovskii, J. Phys. Chem. Sol. **70**, 64 (2009). https://doi.org/10.1016/j.jpcs.2008.09.004
34. F. D. Murnaghan, Amer. J. Math. **59**, 235 (1937). https://doi.org/10.2307/2371405
35. W. Voigt, Lehrbuch der Kristallphysik (Textbook of Crystal Physics) (Springer, Berlin, 1928).
36. A. Reuß, J. Appl. Math. Mech. **9**, 49 (1929). https://doi.org/10.1002/zamm.19290090104
37. M. Islam and M. M. Islam, Chem. Phys. **597**, ID 112805 (2025). https://doi.org/10.1016/j.chemphys.2025.112805
38. M. Islam and M. M. Islam, Chem. Phys. **600**, ID 112917 (2026). https://doi.org/10.1016/j.chemphys.2025.112917
39. F. Mouhat and F. Coudert, Phys. Rev. B **90**, ID 224104 (2014). https://doi.org/10.1103/PhysRevB.90.224104
40. M. Born, Math. Proc. Camb. Philos. Soc. **36**, 160 (1940). https://doi.org/10.1017/S0305004100017138
41. M. Lee and R. S. Gilmore, J. Mat. Sci. **17**, 2657 (1982). https://doi.org/10.1007/BF00543901
42. D. Connétable, Mat. Res. Exp. **3**, ID 126502 (2016). https://doi.org/10.1088/2053-1591/3/12/126502
43. M. M. Islam, H. Mikat, and M. Islam, J. Sci. Res. **18**, 147 (2026). https://doi.org/10.3329/jsr.v18i1.83725
44. M. Islam and M. A. R. Sheikh, Nucl. Mater. Energ. **41**, ID 101734 (2024). https://doi.org/10.1016/j.nme.2024.101734
45. M. R. Talukder and M. R. Islam, Fuel Proc. Tech. **277**, ID 108312 (2025). https://doi.org/10.1016/j.fuproc.2025.108312
46. M. Islam, J. Sci. Res. **15**, 739 (2023). https://doi.org/10.3329/jsr.v15i3.64394